JOURNAL OF COMPUTATIONAL PHYSICS 121, 176–184 (1995)

A Comparison of ENO and TVD Schemes for the Computation of Shock–Turbulence Interaction

RALF HANNAPPEL

Adam Opel AG, Technical Development Center Europe, TEZ 83-10, D 65423 Rüsselsheim, Germany

THOMAS HAUSER AND RAINER FRIEDRICH

Lehrstuhl für Fluidmechanik, Arcisstrasse 21, D-80290 Munich, Germany

Received November 16, 1990; revised September 6, 1994

A quantitative analysis of solutions to the Euler equations of fluid dynamis with the MUSCL, ENO–Harten, and efficient ENO–Shu algorithms is performed. Investigations of different test problems in one and two dimensions are presented. These are chosen as to model the shock–turbulence interaction in fluid dynamical systems. The notion of subcell resolution developed by Harten for the ENO schemes clearly improves the solution in one dimension; however, the effect is less prominent in a Strang-type extension to two dimensions. Our results confirm the superiority of the ENO schemes over the MUSCL approach in solving problems of flow fields with discontinuities which, at the same time, contain fine structure in its smooth parts.

1. INTRODUCTION

The direct numerical simulation of compressible turbulent flow interacting with a shock needs accurate and efficient schemes for the integration of the Navier–Stokes equations. On the one hand one has to resolve the fine structure in the smooth flow field; on the other hand one must capture a shock very accurately not to produce oscillations that may be misinterpreted as enhanced turbulence. There are actually only few numerical schemes that could handle both points satisfactorily. Spectral codes and compact schemes will not satisfy the latter criterion unless the shock is very broad; shock-fitting approaches are possible but very complicated because of the corrugated structure of the shock. Only high resolution schemes like the TVD–MUSCL approach of van Leer [11] or the ENO approach of Harten [7] seem to be able to handle these sorts of problems. In our investigation we used ENO schemes up to fourth order to demonstrate their superiority over TVD schemes for calculations of fluid flows with a spatial structure. We compare results in one and two dimensions of a TVD algorithm, ENO schemes with/without subcell resolution and the efficient implementation of the ENO approach. They are used to approximate systems of hyperbolic conservation laws of the type

$$\mathbf{u}_t + \sum_{i=1}^{d} \mathbf{f}_i(\mathbf{u})_{x_i} = 0, \quad t > 0, \tag{1}$$

$$\mathbf{u}(\mathbf{x}, 0) = \mathbf{u}_0(\mathbf{x}), \tag{2}$$

where $\mathbf{u} = (u_1, \ldots, u_s)^T$, $\mathbf{x} = (x_1, \ldots, x_d)^T$, d is the dimension of the problem, and s is the number of independent variables. We use bold face letters to denote the vector quantities and plain letters for scalar quantities. The system of Eq. (1) is hyperbolic in the sense that $A_i(\mathbf{u}) = \partial \mathbf{f}_i / \partial \mathbf{u}$ has real eigenvalues and a set of linearly independent eigenvectors.

The TVD scheme used for comparison is a MUSCL scheme by Colella [2] which we will call TVD–MUSCL in the following. It is a modification of van Leer's and Woodward's original algorithms in [11, 12]. A numerical method is called total variation diminishing (TVD), if the following inequality holds for scalar conservation laws

$$TV(U^{n+1}) \le TV(U^n) \tag{3}$$

with U^n being the cell average of any grid function at the nth time step. The total variation of a discrete function u_i at site i being defined as

$$TV(u) = \sum_i |u_i - u_{i-1}|. \tag{4}$$

In the TVD–MUSCL approach the piecewise linear reconstruction $\tilde{u}^n(x, t_n)$ of the cell averages U^n in the cell ensures that

$$TV(\tilde{u}^n(x, t_n)) \le TV(U^n) \tag{5}$$

It can be shown, that with this condition being fulfilled the scheme is TVD for scalar conservation laws. To guarantee this property in flows with discontinuities, slope limiters are introduced. They, however, reduce the accuracy of the approximation near local extrema and discontinuities. In the TVD–MUSCL approach, the linear distribution $\tilde{u}^n(x, t_n)$ of the vari-

0021-9991/95 $12.00

ables in the cells and the choice of the limiters are obtained using Colella's algorithm.

The ENO algorithms were taken from Harten's publications [7, 8] and the efficient implementation of Shu from [15, 16]. The introduction of the powerful notion of subcell resolution (SR) of Harten [9] is used to steepen the contact discontinuities in solutions of the Euler equations. The polynomial $\tilde{u}^n(x, t_n)$ in the ENO reconstruction obeys the relation

$$TV(\tilde{u}^n(x, t_n)) \leq TV(U^n) + \mathbb{O}(h^r), \tag{6}$$

where $\tilde{u}^n(x, t_n)$ in (6) denotes a piecewise polynommial reconstruction of order $(r - 1)$, h is the grid spacing. This implies that the reconstruction is essentially non-oscillatory, allowing oscillations of $\mathbb{O}(h^r)$.

Both approaches try to obtain a more accurate representation of the initial distribution by a polynomial expansion of the mean values in the cell. The basic difference of the two is obvious from Eqs. (5) and (6). The use of slope limiters in the TVD–MUSCL case results in the loss of the extra term present in (6). The necessity of limiters in the MUSCL case leads to the clipping of extrema due to their inability to distinguish between local extrema and discontinuities. An explanation for the clipping phenomenon is the fact that all standard limiters consider only the ratio of two differences which does not provide enough information to discriminate a local extremum from a discontinuity.

In the ENO case though, the total variation is bounded by means of the adaptive stencil technique. The polynomial is thereby generated through an adaptive stencil via the divided differences in such a way, that only those points contribute to the approximation, through which the polynomial is the "smoothest." Due to this adaptivity the high order accuracy of the method can be obtained right up to discontinuities in the computational domain and does not result in the clipping of local extrema. It should be noted that it is possible to convert a second-order efficient ENO scheme to a well known TVD scheme by substituting the stencil selection algorithm with the minmod function (see [16]). Inherent to the construction of the ENO algorithm is the fact, that it can, in principle, be extended to any desired order of accuracy. While the original ENO scheme of Harten uses a reconstruction procedure to evaluate point values from cell averages, the efficient implementation applies the adaptive stencil idea directly to the numerical fluxes and is thereby supposed to save lots of effort for a multi-dimensional implementation.

To obtain two-dimensional results we used the fractional step time-splitting method of Strang [17] in the TVD–MUSCL approach of Colella and in the ENO implementation of Harten, while in the efficient ENO case we used the algorithm described in [15, 16] with a TVD–Runge–Kutta time integration.

In the next section we will briefly review the numerical procedures of the ENO algorithms used in this paper. We will display errors of some numerical solutions in Section 3.

2. IMPLEMENTATION OF THE ENO SCHEMES

We briefly describe the implementation of the ENO schemes of Harten ("ENO–Harten" in the following) taken from his original paper [7], the implementation of the subcell resolution (SR) as developed in [9], and the efficient implementation of the ENO scheme ("ENO–Shu") of [15, 16]. The TVD–MUSCL approach of Colella need not be described again, but is given in detail in the original paper of 1985 [2].

General Remarks

The basic difference between other high resolution schemes and the ENO approach lies in the application of an adaptive stencil, that adjusts to the smoothness of the solution. The stencil chooses points that will contribute to the computation of fluxes over cell interfaces for the next time step in a nonlinear manner, dependent on the instantaneous solution. Its criterion is the smoothness of the field, which is determined by the computation of divided differences. In smooth fields these are a measure for the derivative of the solution, while in fields with discontinuities they are of the order of the jump. No limiter functions that would reduce the order of a scheme near such jumps are therefore necessary. The stencil selection algorithm uses enough information to decide whether three differences mimic an extremum or a discontinuity. This gives rise to the property that high order ENO schemes do not clip local extrema and one can obtain oscillation-free solutions near discontinuities.

Implementation of the ENO–Harten Algorithm

The original ENO–Harten scheme uses piecewise smooth polynomials of high order to obtain an essentially non-oscillatory reconstruction of the solution $u(x, t_n)$ in the cell. After transforming the conservative variables into the characteristic directions we interpolate the characteristic components, because this approach gives rise to a smoother representation of the solution than using the conservative components directly (see numerical experiments in [7]). By means of a Cauchy–Kowalewski procedure, time derivatives of the conservative varibles are expressed as functions of spatial derivatives. Using these in a Taylor expansion of the primitive variables in time yields Riemann problems at time levels between the old and new time step t^n and t^{n+1}, respectively. The resulting fluxes $f^{\mathrm{ENO}}_{j+1/2}(t^n < t < t^{n+1})$ are integrated by the Gaussian integration technique to obtain the time averaged flux in the time interval $\Delta t = t^{n+1} - t^n$. Updating the next time level is performed by an Euler time step. The solution of Riemann problems at the cell interface is in all ENO computations approximated using Roe's averaging. A correction to the flux according to Harten and Hyman [10] is added to omit entropy violation.

Implementation of the Subcell Resolution

In the SR case which was originally designed for one space dimension special attention is being taken of the detection and

resolution of contact discontinuities. Its extension to higher dimensions is a tedious task. At present it is not clear how to extend the concept of the subcell resolution to multi-dimensional problems. In one dimension it is performed by extrapolating the polynomials to the left and to the right of the cell up to a position z into the cell giving a second polynomial representation. z is determined by setting the average value of the characteristic variable equal to the integral of the two polynomials over the cell. A flux that is being added to the ENO–Harten flux stems from the difference of this polynomial representation inside the cell and the original one. The detection of contact discontinuities is done using the derivative of the polynomial multiplied by the eigenvector that corresponds to the linearly degenerate characteristic field. [1]One could in principle extend such a modification to the other characteristic fields as well; the computational effort, however, is too high compared to the gain in accuracy.

Implementation of the Efficient ENO Scheme

We want to emphasize that for Shu's ENO schemes efficiency means ease of implementation especially for multi-dimensional cases. In the efficient ENO algorithm the reconstruction of point values from cell averages is overcome by applying the adaptive stencil directly to the fluxes. So not only this step is omitted, but also having to solve a Riemann problem. We used the ENO–RF algorithm of [16] in the following, which is a combination of the ENO–Roe and ENO–LLF (local Lax–Friedrichs) algorithms. In the ENO–Roe case the fluxes are transformed into the characteristic directions by multiplying them with the matrix of left-eigenvectors, that was obtained by Roe averaging the conservative components. After determining the (local) wind direction, the first point of the stencil is chosen in the upwind direction to obtain stability. The further choice of the stencil is done in the ENO–Harten manner. After multiplying the interpolated fluxes at the cell interfaces with the right eigenvectors, an updating is made by a TVD Runge–Kutta time integration scheme developed by Shu [15] with an accuracy up to fourth order. This scheme is labeled TVD, because it has been shown (see [15]) that it does not increase the total variation of the spatial part under a suitable CFL restriction. If "expansion shocks" occur in single cells, the flux is modified according to the local Lax–Friedrichs (LLF) algorithm of [16]. The flux vector is thereby split into the sum of two fluxes $f^{\pm}$ at each site such that the matrix of right-/left-eigenvectors has only positive/negative eigenvalues. Projection into the characteristic directions and the choice of the stencil then follow as outlined above for each of the two fluxes. The combination of those two algorithms in the ENO–RF implementation was chosen, because it is expected to provide the lowest possible numerical viscosity among the efficient ENO schemes at the same time, omitting the entropy violation by means of switching to the LLF-flux at sign changes of the eigenvalues of $\partial \mathbf{f}_i/\partial \mathbf{u}$. The computational amount increases compared to the ENO–Roe algorithm alone as one has to compute the divided differences not only for the fluxes but additionally for the components $\mathbf{u}$.

[1] We want to mention at this point that there is a typographical error in [9] in Eqs. (6.10a±). There must be a $\tau\delta_j$ on the left-hand side instead of a δ_j.

3. NUMERICAL RESULTS

We use the notation ENO/r for approximations to the differential equation (1) with the ENO–Harten scheme, where $r = 2, 3, 4$ refers to the order of the approximation. ENO/r/SR denotes the ENO scheme of order r with subcell resolution. For the efficient approximation with the ENO–Shu scheme we choose the notation to be EENO/r (efficient ENO). The CFL number we used in all calculations with the exception of the EENO/r case is 0.9. In the latter situation we had to reduce the CFL number to 0.5 in order to obtain oscillation-free results. As a measure of error in one dimension we take the

$$l_2\text{-norm: } \left\{ \frac{1}{N} \cdot \sum_{i=1}^{N} (v_i - u(x_i, t))^2 \right\}^{1/2} \tag{7}$$

with N denoting the number of grid points in x direction. v_i is the approximation to the exact solution $u(x_i, t)$.

In two dimensions we define it to be

$$l_2\text{-norm: } \left\{ \frac{1}{N_x N_y} \cdot \sum_{i=1}^{N_x} \sum_{j=1}^{N_y} (v_{ij} - u(x_i, y_j, t))^2 \right\}^{1/2}, \tag{8}$$

where N_x, N_y is the number of points in x, y directions, respectively.

Example 1

In this example we consider the one-dimensional problem of [16] solving the Euler equations for a polytropic gas following a γ-law, i.e., Eq. (1) with $d = 1$ and $s = 3$. ρ, q, M, E, and P denote the density, velocity, momentum, total energy, and pressure, respectively; γ is chosen to be 1.4,

$$\mathbf{u} = (\rho, M, E)^{\mathrm{T}}, \quad f(\mathbf{u}) = q\mathbf{u} + (0, P, qP)^{\mathrm{T}}, \tag{9}$$

where

$$P = (\gamma - 1)(E - \tfrac{1}{2}\rho q^2), \quad M = \rho \cdot q. \tag{10}$$

The initial conditions describe the interaction of a Mach 3 shock with a sine wave in the density field, by keeping all other thermodynamic quantities constant; i.e.,

$$\begin{aligned} &\rho = 3.857143, \quad q = 2.629369, \quad p = 10.333333 \quad \text{for } x < -4, \\ &\rho = 1 + \varepsilon \sin 5x, \quad q = 0, \quad p = 1 \quad \text{for } x \geq -4. \end{aligned}$$

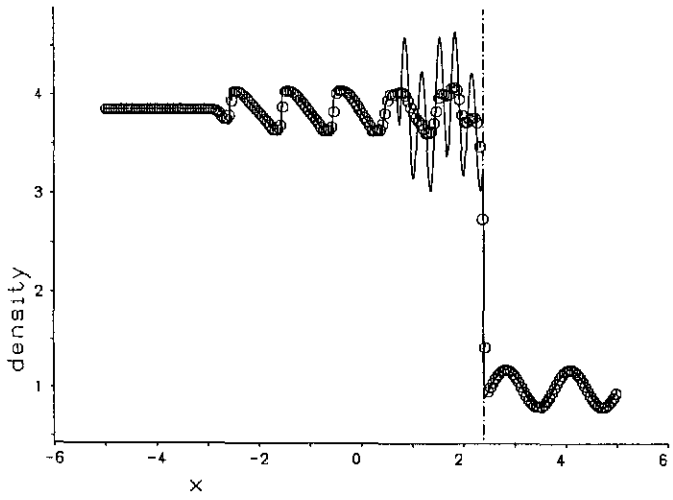

FIG. 1. TVD–MUSCL scheme compared with exact solution.

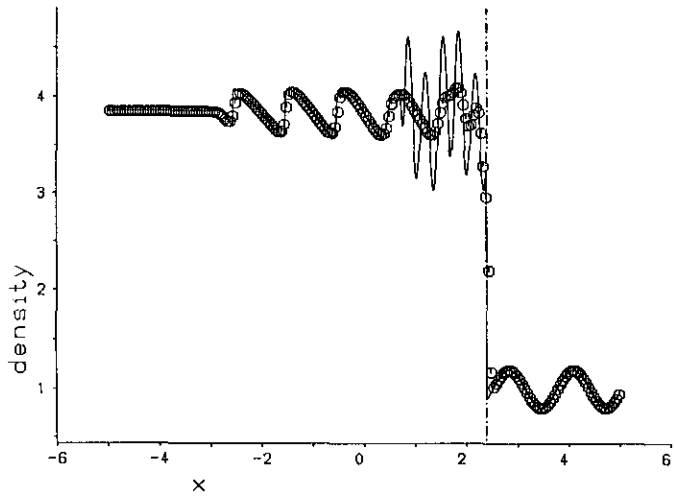

FIG. 3. EENO/2 scheme compared with exact solution.

The results for EENO/2 and EENO/3 were obtained using a CFL number of 0.5; those for EENO/4 were obtained with a CFL number of 0.2. We use $\varepsilon = 0.2$. An analytic linearized solution exists for $\varepsilon \ll 1$ in [14], with which our results are in qualitative agreement. The "exact" answer to the hydrodynamic problem is given by a numerical solution with 1600 points in the interval $[-5; 5]$ (as can also be seen in [16]). All other results shown are obtained using 200 points; the integration time is $t = 1.8$.

In Figs. 1 to 6 plots of the results obtained with the different approximations are shown. In Fig. 1 the damping of the TVD–MUSCL compared to the ENO solutions in Figs. 2–6 can be seen. The strong attenuation of the amplitudes occurs mainly at the first three extrema. The ENO/2 algorithm in Fig. 2 shows—in comparison with the EENO/2 implementation of Fig. 3—a slightly better resolution of these maxima. A comparison of ENO/2/SR in Fig. 4 with ENO/2 and EENO/2 shows a significant improvement. The l_2-norm is 29% lower than the norm for the ENO/2 algorithm and only about 2% higher than that for the fourth-order ENO/4 result, thus showing the excellent performance of the subcell resolution concept in the one-dimensional case.

The approximation with which we obtained the best results in the smooth part of the solution is the fourth-order algorithm of Harten with SR which is shown in Fig. 5. An obvious problem for all schemes in this low resolution remains the proper prediction of the flow behaviour at the position, where the acoustic (fast travelling) and the entropy waves (for the last time) interact, i.e., at $x \approx 0.8$.

The results show, that the TVD–MUSCL scheme has a shock

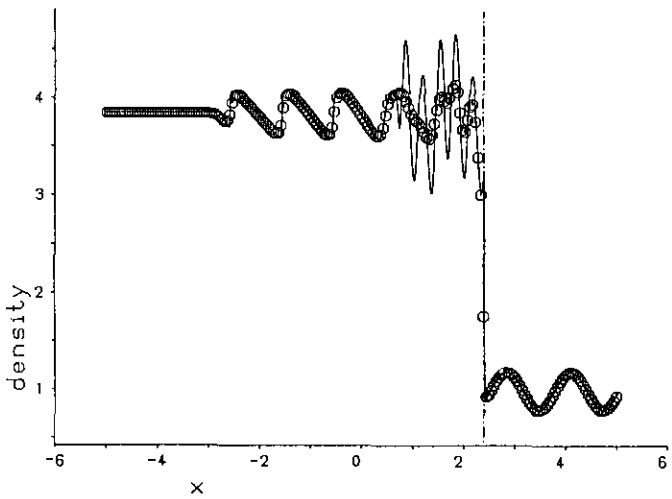

FIG. 2. ENO/2 scheme compared with exact solution.

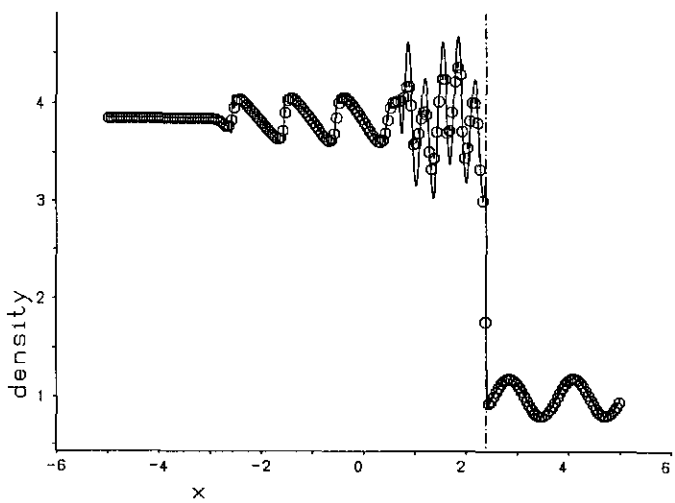

FIG. 4. ENO/2/SR scheme compared with exact solution.

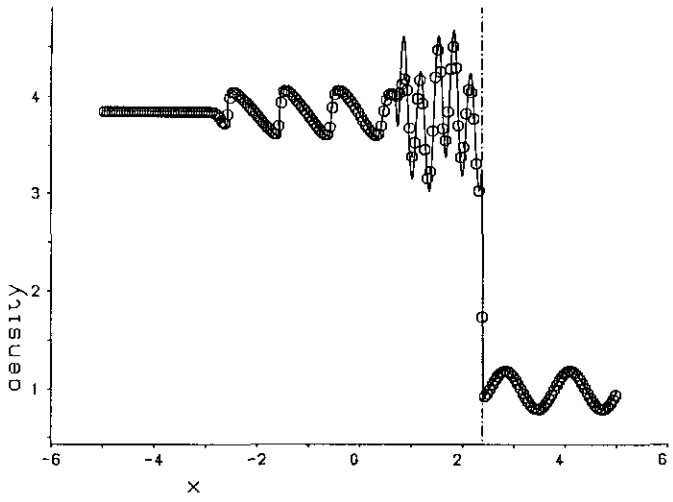

FIG. 5. ENO/4/SR scheme compared with exact solution.

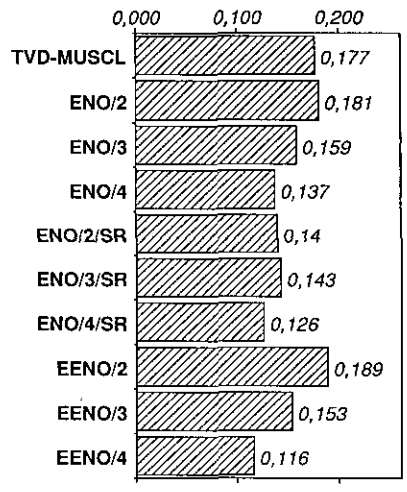

FIG. 7. l_2 norms of the density in the one-dimensional test problem with $\Delta x = \frac{1}{20}$.

profile which is comparatively as steep as the shock profile given by the ENO approximations. The shock-widths produced by all ENO schemes are approximately equal, with the efficient EENO scheme of second-order accuracy giving the worst values. Note, that SR does not improve the shock-thickness (measured in terms of number of grid points), but only leads to a better prediction of the contact discontinuities in the flow field. The shock width is a difficult quantity to define and evaluate in this case. One should also note that there are limiters for the TVD–MUSCL scheme which show overcompression effects and steepen the shock profile even more.

A point we want to stress is the difference between results gained with EENO/4 and ENO/4/SR. In Fig. 7, which contains the l_2-norms the EENO/4 realization has a lower value in the error norm than ENO/4 and ENO/4/SR as well. Despite the higher absolute errors of the efficient implementation in comparison with Harten's algorithms in the smooth part of the solution, we observe this strange result because of the very high derivation of the ENO/4 and ENO/4/SR values from the exact solution at the shock location. The absolute value of the density at one point belonging to the shock is one order of magnitude higher than in the EENO case. This creates an approximately 9% higher value in the l_2-norm of the ENO/4/SR data on the coarse grid.

From these results we conclude that the ENO scheme gives a better representation of the exact solution than the TVD–MUSCL scheme. The efficient implementation of Shu shows slightly better results for the fourth-order case close to the shock than the one of Harten. In the smooth part of the solution, however, the latter represents the physics more accurately.

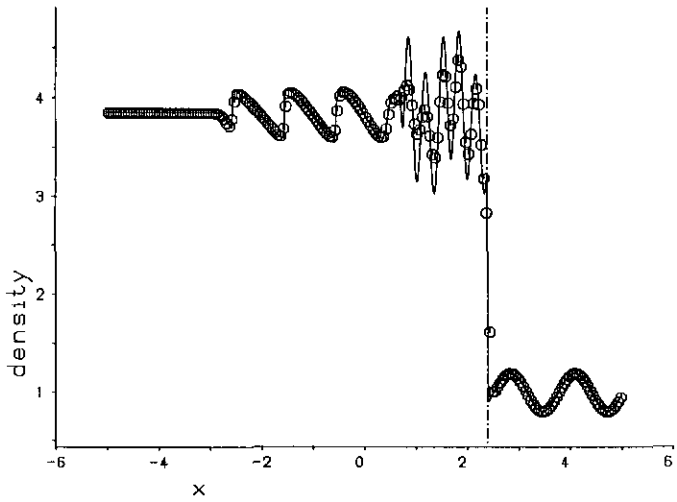

FIG. 6. EENO/4 scheme compared with exact solution.

Two-Dimensional Problem

In the case of the original ENO/r scheme with/without SR in two dimensions we used the fractional step time-splitting algorithm of [17]. This implementation in not a really two-dimensional implementation as the one described in [6 or 1]. The fractional step method approximates the solution only up to $O(\Delta t^2)$. In case of higher order approximations, however, the one-dimensional spatial operators will be approximated to a higher degree of accuracy. This is confirmed by our results. For the EENO/r scheme the one-dimensional algorithm is applied to each of the terms $\mathbf{f}_i$ in (1) while keeping all other variables fixed (see [16]). Another remark we want to add is the fact that, concluding from the numerical experiments we performed, we expect the phase errors in the case of structured fields to depend on the order of the approximation in space and time. This, on the other hand, will be crucial for an appropriate description of turbulent flows.

In our example the Euler equations in two dimensions are

given by Eq. (1) with $d = 2$ and $s = 4$ (we will use x and y instead of x_1 and x_2) with the definitions

$$\mathbf{u} = (\rho, M_x, M_y, E)^T, \tag{11}$$

$$\mathbf{f}_x(\mathbf{u}) = q_x\mathbf{u} + (0, P, 0, q_xP)^T, \quad \mathbf{f}_y(\mathbf{u}) = q_y\mathbf{u} + (0, 0, P, q_yP)^T, \tag{12}$$

where

$$P = (\gamma - 1)\left(E - \frac{1}{2}\rho q^2\right), \tag{13}$$

$$q^2 = q_x^2 + q_y^2, \quad M_x = \rho q_x, \quad M_y = \rho q_y, \tag{14}$$

and

$$c^2 = (\gamma - 1)\cdot\left(H - \frac{1}{2}q^2\right), \quad H = \frac{E + P}{\rho}. \tag{15}$$

The symbols denote the same quantities as those used in the previous example. The indices x and y refer to their components in the corresponding directions. The eigenvalues of $\partial\mathbf{f}_x/\partial\mathbf{u}$ are

$$\lambda_1 = q_x - c, \quad \lambda_2 = \lambda_3 = q_x, \quad \lambda_4 = q_x + c. \tag{16}$$

The matrix, the columns of which are the right eigenvectors $\mathbf{r}_k$, is

$$R_F = (\mathbf{r}_1, \mathbf{r}_2, \mathbf{r}_3, \mathbf{r}_4) = \begin{pmatrix} 1 & 1 & 0 & 1 \\ q_x - c & q_x & 0 & q_x + c \\ q_y & q_y & 1 & q_y \\ H - q_xc & \frac{1}{2}q^2 & q_y & H + q_xc \end{pmatrix}, \tag{17}$$

while the matrix, the rows of which are the left eigenvectors $\mathbf{l}_k$, is

$$L_F = \begin{pmatrix} \mathbf{l}_1 \\ \mathbf{l}_2 \\ \mathbf{l}_3 \\ \mathbf{l}_4 \end{pmatrix} = \frac{1}{2}\begin{pmatrix} b_2 + q_x/c & -1/c - b_1q_x & -b_1q_y & b_1 \\ 2(1 - b_2) & 2b_1q_x & 2b_1q_y & -2b_1 \\ -2q_y & 0 & 2 & 0 \\ b_2 - q_x/c & 1/c - b_1q_x & -b_1q_y & b_1 \end{pmatrix}, \tag{18}$$

with

$$b_1 = \frac{(\gamma - 1)}{c^2}, \quad b_2 = \frac{1}{2}q^2b_1. \tag{19}$$

The results of $\partial\mathbf{f}_y/\partial\mathbf{u}$ are obtained by exchanging q_x and q_y in the above vectors.

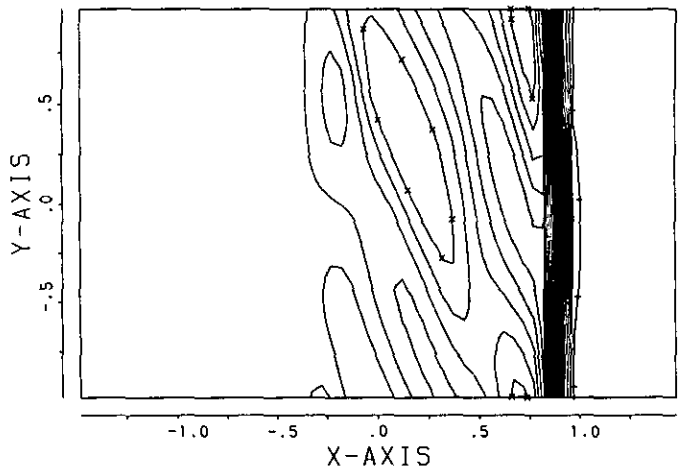

FIG. 8. ENO/2 contour plot of the density at $t = 0.2$. Grid spacing $h = \frac{1}{20}$.

Example 2

In this last example we consider a vorticity wave interacting with a shock. This test problem was used in [18] and was computed with the efficient ENO scheme in [16] to demonstrate the capability of the ENO schemes especially for shock–turbulence interactions. In this problem a Mach 8 shock initially at $x = -1$ is moving to the right into a gas with the following flow variables: $p_1 = 1$, $\rho_1 = 1$, and $q_x = -(c_1/p_1)\sin\vartheta_1\cos(xk_1\cos\vartheta_1 + yk_1\sin\vartheta_1)$, $q_y = (c_1/p_1)\cos\vartheta_1\cos(xk_1\cos\vartheta_1 + yk_1\sin\vartheta_1)$ with $k_1 = 2\pi$, $\vartheta_1 = \pi/6$. The wavelength of the vorticity wave in the y direction being 2. The index 1 in the initial conditions denotes the preshock situation. The domain of computation is $[-1.5; 1.5] \times [-1; 1]$. Periodic boundary conditions are used in the y direction. In Figs. 8 and 9 contour plots of the density are shown at time $t = 0.2$ for two different spatial resolutions. The ENO/2 algorithm is used to integrate the Euler equations. The grid spacing in x and y direction is $h = \frac{1}{20}$ in

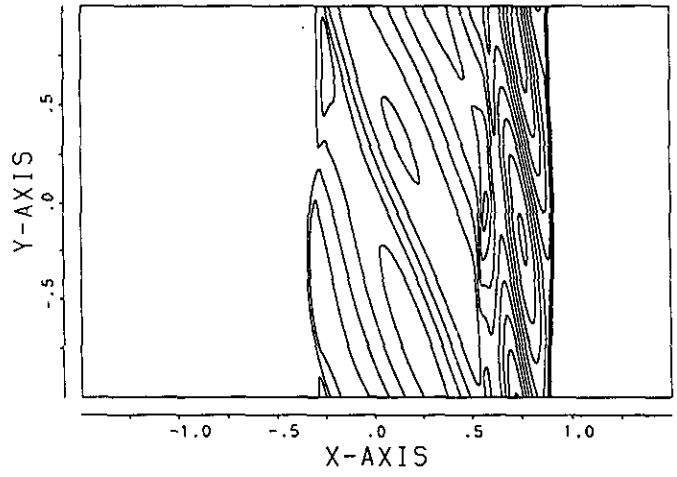

FIG. 9. ENO/2 contour plot of the density at $t = 0.2$. Grid spacing $h = \frac{1}{320}$.

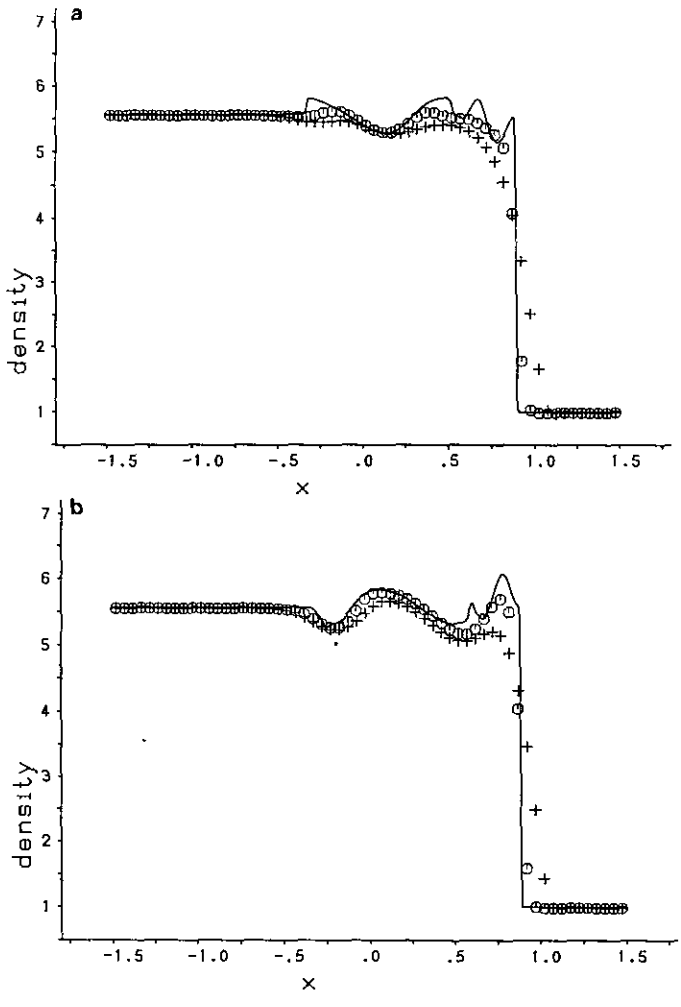

FIG. 10. Cut at $y = -0.525$ (a) and $y = 0.525$ (b). Comparison of the TVD–MUSCL and ENO/2 results with a high-resolution run of 960×640 grid points. Crosses denote the TVD–MUSCL, circles denote the ENO/2, and the solid line is the exact solution.

Fig. 8 and $h = \frac{1}{320}$ in Fig. 9. Forty-one contours are displayed from 1.030 to 6.100, with a spacing of 0.130. The maximum on the coarse grid run is only 5.710 (marked with "x"), because of the lower resolution.

Figure 9 represents the numerical solution we consider to be "exact," obtained on a 960×640 grid. This means, that a further refinement of the grid has led to practically the same solution everywhere in the field. We display the density, because the SR is applied only to perturbations that are transported with the fluid velocity, thus improving only, e.g., entropy, and thereby density discontinuities. To compare the different schemes we consider the density profiles at constant y. In Figs. 10a and b a cut through the computational regime at $y = -0.525$ and $y = 0.525$ is shown. The crosses denote the solution obtained with the TVD–MUSCL algorithm on a mesh with 60×40 grid points, the circles denote the ENO/2 results. The solid line corresponds to the "exact" solution of Fig. 9 with 960×640 grid points. If we compare the two results, it is obvious that the TVD–MUSCL scheme dampens the maxima more than the corresponding ENO approximation. The shock is broadened up to six mesh points, thus giving a worse shock representation than the ENO/r schemes. Figures 11a and b confirm the validity of this statement also for the EENO/r results. We ran the computations for the TVD–MUSCL scheme also with a grid of 240×160 points which naturally gave a better representation of the shock. In the wavy part of the density field, however, it is only roughly 10% better than the ENO/2 result on the 60×40 grid. This already shows the excellent performance of the ENO algorithm for this sort of two-dimensional problems. This statement is supported by the l_2 norms in Table I.

If we increase the order of the approximation, we get a better representation of the solution. In Fig. 12a and b we plotted the

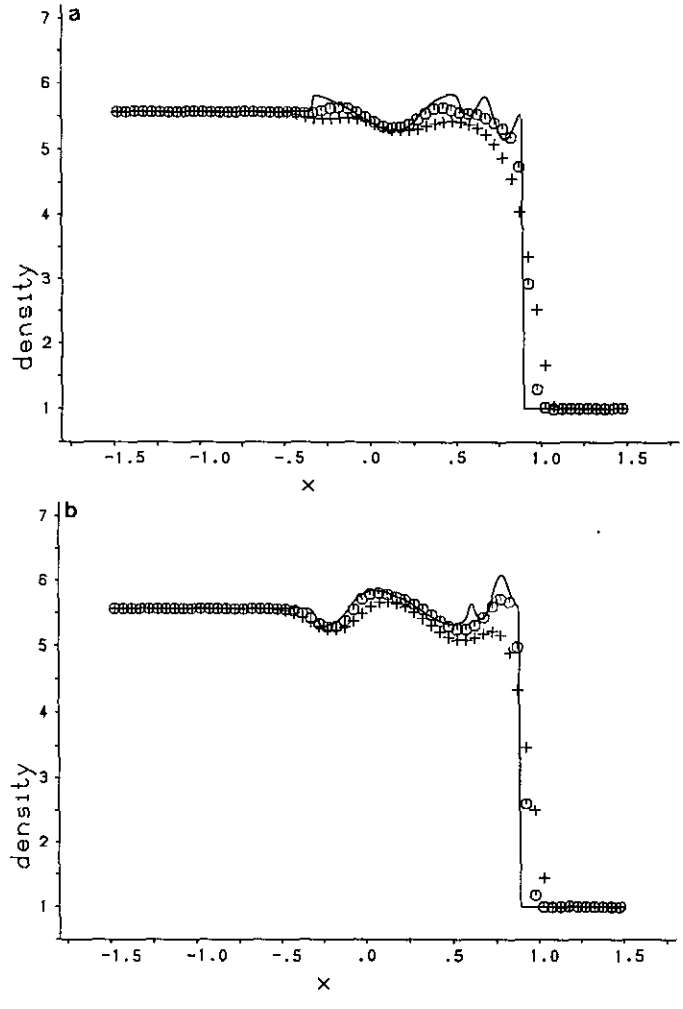

FIG. 11. Cut at $y = -0.525$ (a) and $y = 0.525$ (b). Comparison of the TVD–MUSCL and EENO/2 density results with a high-resolution run of 960×640 grid points. Crosses denote the TVD–MUSCL, circles denote the EENO/2, and the solid line is the exact solution.

TABLE I

l_2 Norms of the Density in the Case of a Vorticity-Wave Interacting with a Shock

	$y = -0.525$	$y = 0.525$	$\forall (x, y)$
TVD–MUSCl	0.456	0.468	0.466
ENO/2	0.227	0.232	0.242
ENO/2/SR	0.227	0.235	0.245
ENO/3	0.214	0.240	0.239
ENO/3/SR	0.214	0.243	0.238
ENO/4	0.200	0.187	0.209
ENO/4/SR	0.212	0.242	0.238
EENO/2	0.280	0.235	0.274
EENO/3	0.290	0.233	0.280
EENO/4	0.384	0.331	0.371

same cuts for the EENO/4 and ENO/4 data. Despite of the fourth-order TVD time discretization in the EENO case the approximation turns out to be hardly better than in the second-order in time ENO approach. If we turn on the SR in the ENO/2/SR computation (see Fig. 13a), the scheme shows an overcompression effect at $y = -0.525$ and $x \approx 0.525$. This is the region, where three waves interact, namely the entropy, acoustic, and transmitted vorticity wave. The failure of the SR approach in this case may be due to the fact that the algorithm is basically 1D and cannot simply be extended to a truly two-dimensional implementation. In Figs. 13a and b the direct comparison of the ENO/2 with ENO/2/SR results shows as well that an extension of the SR to two dimensions via Strang's dimensional splitting does not enhance the quality of the solution. This is confirmed by the l_2 norms in Table I which do not decrease with the SR being added. A computation using a fourth-order ENO scheme with SR further reduces the quality

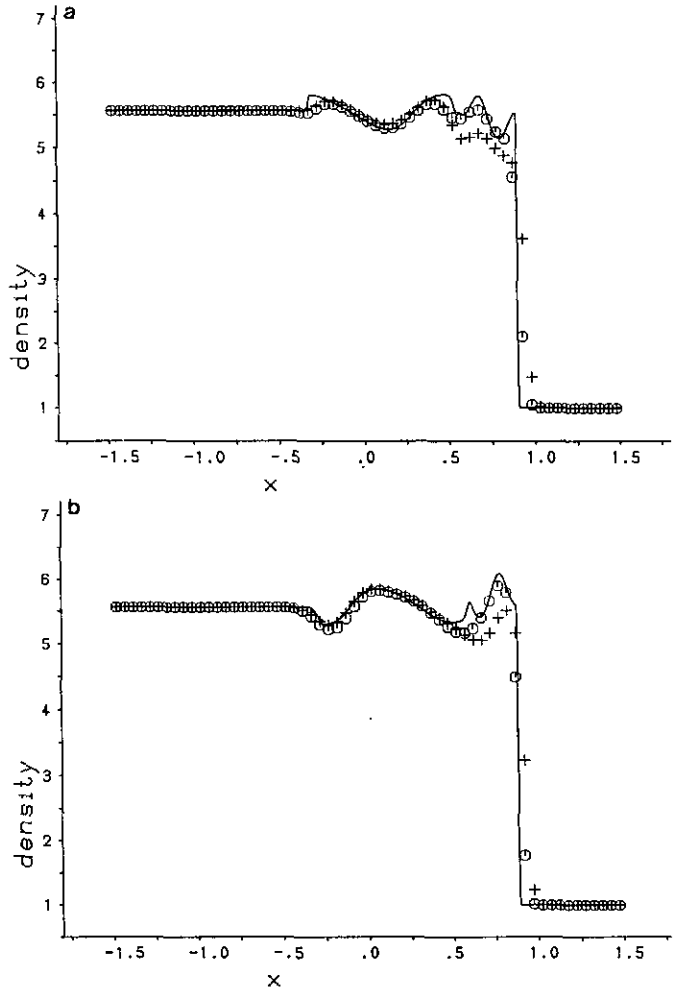

FIG. 12. Cut at $y = -0.525$ (a) and $y = 0.525$ (b). Comparison of the EENO/4 and ENO/4 density results with a high-resolution run of 960 × 640 grid points. Crosses denote the EENO/4, circles denote the ENO/4, and the solid line is the exact solution.

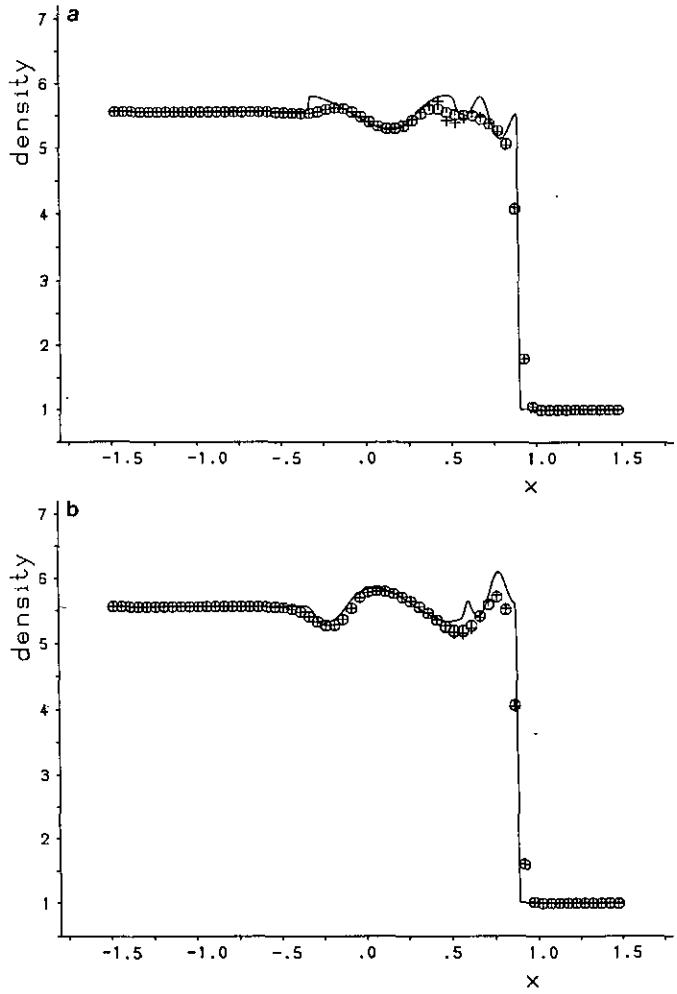

FIG. 13. Cut at $y = -0.525$ (a) and $y = 0.525$ (b). Comparison of the ENO/2/SR and ENO/2 density results with a high-resolution run of 960 × 640 grid points. Crosses denote the ENO/2/SR, circles denote the ENO/2, and the solid line is the exact solution.

of the result. A full multi-dimensional implementation of the SR algorithm would be desirable.

4. CONCLUSIONS

We have investigated the behaviour of ENO algorithms designed by Harten [7] and Shu [16] to solve the Euler equations of fluid dynamics in comparison to a TVD scheme. The TVD algorithm chosen was that of Colella [2]. Two of the test problems modelled the shock–turbulence interaction. In the example of an incoming wave, namely a density wave in one dimension and a vorticity wave in two dimensions, interacting with a shock, we found, that the TVD–MUSCL approach does not provide satisfactory results. It leads to a sharp shock without oscillations at the expense of the accuracy in the smooth part of the solution. This accuracy, however, is necessary for the direct numerical simulation of compressible turbulence. The ENO schemes provide higher accuracy compared to the TVD–MUSCL approach in the smooth parts while preserving sharp shock profiles. Comparing the different implementations of the ENO method, the ENO schemes of Harten are more accurate than the EENO schemes. This advantage is outweighed by the ease of multi-dimensional implementation of the efficient ENO schemes. A true two-dimensional implementation of the ENO schemes [1] is much more laborious. Applying the subcell resolution approach in one dimension we confirmed the extremely promising results of Harten and Shu. Its simple implementation in two dimensions via Strang's fractional steps method showed no significant improvement of the numerical results, being not at all comparable to those achieved in the one-dimensional example. We tried to confirm this by computing the l_2 norms of the different schemes in one and two dimensions for the different test cases.

A computation of the first test problem using an implementation of the TVD–PPM method of [4] by Gathmann [5] did show some improvement over the TVD–MUSCL scheme, but still lead to results worse than those of the ENO scheme. With respect to the shock–turbulence interaction problem we finally conclude that the ENO schemes are more reliable in predicting the complicated flow structure than TVD schemes.

ACKNOWLEDGMENTS

The financial support of this work by the German Research Association (DFG) under the project numbers Fr 478/11-1 and SFB 255, project A6 is gratefully acknowledged.

REFERENCES

1. J. Casper and H. L. Atkins, *J. Comput. Phys.* **106,** 62 (1993).
2. P. Colella, *SIAM J. Sci. Stat. Comput.* **6,** 1 (1985).
3. P. Colella, Report LBL-17023 (unpublished).
4. P. Colella and P. R. Woodward, *J. Comput. Phys.* **54,** 174 (1984).
5. R. J. Gathmann, Institut de Méchanique de Grenoble, B.P. 53 x, 38041 Grenoble Cédex, France, private communication, 1991.
6. A. Godfrey, C. Mitchell, and R. Walters, *AIAA J.* **9,** 1634 (1993).
7. A. Harten, B. Enquist, S. Osher, and S. Chakravarty, *J. Comput. Phys.* **71,** 231 (1987).
8. A. Harten, "Preliminary Results on the Extension of ENO Schemes to two dimensional problems," in *Proceedings, International Conf. on Hyperbolic Problems, Saint-Etienne, January 1986* (unpublished).
9. A. Harten, *J. Comput. Phys.* **83,** 148 (1989).
10. A. Harten and J. M. Hyman, *J. Comput. Phys.* **50,** 235 (1983).
11. B. van Leer, *J. Comput. Phys.* **32,** 101 (1979).
12. B. van Leer and P. D. Woodward, "The MUSCL Code for Compressible Flow: Philosophy and Results," in *Proceedings, TICOM Conference in Austin, Texas, 1979* (unpublished).
13. R. LeVeque, *Numerical Methods for Conservation Laws* (Birkhäuser, Basel, 1990).
14. J. F. MacKenzie and K. O. Westphal, *Phys. Fluids* **11,** 2350 (1968).
15. C.-W. Shu and S. Osher, *J. Comput. Phys.* **77,** 439 (1988).
16. C.-W Shu and S. Osher, *J. Comput. Phys.* **83,** 32 (1989).
17. G. Strang, *SIAM J. Numer. Anal.* **5,** 506 (1968).
18. T. Zang, M. Hussaini, and D. Bushnell, *AIAA J.* **22,** 13 (1984).